Direct Bundle Simulation approach for the compression molding process of Sheet Molding Compound

N. Meyer[a,*], L. Schöttl[b], L. Bretz[c], A. N. Hrymak[d], L. Kärger[a]

[a] *Karlsruhe Institute of Technology, Institute of Vehicle System Technology, Karlsruhe, Germany*

[b] *Karlsruhe Institute of Technology, Institute for Applied Materials, Karlsruhe, Germany*

[c] *Karlsruhe Institute of Technology, Institute of Production Science, Karlsruhe, Germany*

[d] *Western University, Dept. of Chemical & Biochemical Engineering, London (ON), Canada*

Abstract

The manufacturing process of Sheet Molding Compounds (SMC) induces a reorientation of fibers during the flow, which influences local properties and is of interest for structural computations. Typically, the reorientation is described with an evolution equation for the second order fiber orientation tensor, which requires a closure approximation and multiple empirical parameters to describe long fibers. However, CT scans of SMC microstructures show that fiber bundles stay mostly intact during molding. Treating hundreds of fibers in such a bundle as one instance enables direct simulation on component scale. This work proposes a direct simulation approach, in which bundle segments experience Stokes' drag forces and opposing forces are applied to the fluid field. The method is applied to specimens with a double-curved geometry and compared to CT scans. The Direct Bundle Simulation provides increased accuracy of fiber orientations and enables prediction of fiber-matrix separation with affordable computational effort at component scale.

Keywords: Process simulation, CT analysis, Compression molding, Discontinuous reinforcement

*nils.meyer@kit.edu

1. Introduction

Sheet Molding Compound (SMC) is a composite material with thermoset matrix material and discontinuous glass or carbon reinforcement fibers. SMC compression molding is an economic process to mass produce complex parts with considerably higher fiber lengths compared to injection molding. Typical parts include automotive body panels due to high surface qualities and in-mold coating capability.

The mechanical properties of SMC depend on local fiber orientation and fiber volume fraction, which can change significantly during flow. However, these properties are difficult to determine after molding, and predicting these properties in the early development process can reduce expensive corrections of mold design. Additionally, utilization of process induced fiber orientations improves the predictive quality of structural simulations [1].

The production of SMC typically starts with the production of semi-finished sheets on an SMC line. The first step is the application of resin to a carrier foil. Chopped fibers fall on this carrier foil in a random transversely isotropic orientation. Afterwards, a second carrier foil is placed on top of the first carrier foil and both of them run through sets of rolls that ensure proper impregnation of the fibers. Then, the material is coiled and stored. The viscosity increases in a maturing process. After maturing, the foils are removed and the material can be cut and stacked to an initial charge for molding. This initial charge has room temperature and is placed into a mold at elevated temperature ($\approx 150\,°C$). The mold is closed and SMC flows with its fibers in a complex shape. The mold can be opened after a few minutes of curing and the final part is released.

SMC rheology was first described with generalized Hele-Shaw type models treating SMC as a one-phase material [2]. Barone and Caulk [3] developed a model with lubrication layers at the mold and a central plug flow. This approach was extended by several authors [4–7].

Fiber reorientation is typically modeled based on fiber orientation tensors introduced by Advani and Tucker [8] as

$$\mathbf{A} = \int_S \mathbf{p} \otimes \mathbf{p} \ \Psi(\mathbf{p}) \ \mathrm{d}p \tag{1}$$

and

$$\mathbb{A} = \int_S \mathbf{p} \otimes \mathbf{p} \otimes \mathbf{p} \otimes \mathbf{p} \ \Psi(\mathbf{p}) \ \mathrm{d}p. \tag{2}$$

Here, $\mathbf{p}$ describes a fiber direction and $\mathrm{d}p$ is the surface element on a unit sphere $S := \{\mathbf{p} \in \mathbb{R}^3 : \|\mathbf{p}\| = 1\}$. These fiber orientation tensors $\mathbf{A}$ and $\mathbb{A}$ represent the second and fourth moment of the fiber orientation distribution function $\Psi(\mathbf{p})$ and thus are a statistical representation of the microstructure. The evolution of the second order fiber orientation tensor $\dot{\mathbf{A}}$ is often described with equations that are based on Jeffery's pioneering work [9]. Assuming that fibers have a large aspect ratio, his result may be written as

$$\dot{\mathbf{A}} = \nabla\mathbf{v} \cdot \mathbf{A} + \mathbf{A} \cdot (\nabla\mathbf{v})^\top - \mathbb{A} : \left(\nabla\mathbf{v} + (\nabla\mathbf{v})^\top\right) \tag{3}$$

for a given velocity gradient $\nabla\mathbf{v}$. Several empirical modifications have been introduced to his work to account for fiber interactions [10], experimentally observed orientation delays [11] and anisotropic diffusivity [12]. These models require a closure of the fourth order fiber orientation tensor $\mathbb{A}$, which can be expressed as an approximation only. Additionally, these models require the fiber length to be much shorter than structural features of the part (scale separation), which does not hold in a lot of cases for SMC.

As an alternative to these statistical descriptions, several authors have developed models for single flexible fibers based on inextensible threads [13], bead chains [14] and linked rigid bodies [15–18]. Typically, these models use lubrication theory and contact formulations to model fiber-fiber interactions [19, 20] as well as hydrodynamic drag forces to describe the long range interaction between fluid and fiber [21, 22]. Two-way coupling using a field of body forces was presented by Lindström and Uesaka [23, 24] to conserve momentum in the direct bundle simulation. However, they utilize the drag of prolate spheroids, which leads to a total drag force on a fiber that depends on discretization [25]. Direct models have been utilized in representative volume elements to determine rheological properties [26, 27], contact properties in microstructures [28] and parameters of macroscopic fiber orientation models [21]. This approach of "computational rheometry" has also been applied to SMC represented as a planar network of fiber bundles that interact through local shear forces at contact points [29–31].

The application of direct fiber simulations at the component scale has been reported only scarcely due to the sheer number of fibers and a reduced number of fibers is typically computed. A bead chain model was used by Kuhn et al. [32] and constrained beams were suggested by Hayashi et al. [33] at this scale. A commercial tool utilizing direct fiber simulation is 3D TIMON by TORAY Engineering. However, the tool neglects anisotropy and two-way coupling, as it is run after the determination of the flow field. Additionally, it does not include any interactions between fibers and it seems to use only a small subset of test fibers.

The evolution of the fiber microstructure is a complex phenomenon. However, CT scans in this work show that most fiber bundles in the core of a part stay intact during SMC molding, while few bundles at the mold surface are disentangled. This observation is also reported in literature [34–37]. This behavior allows at least in some flow situations the simplifying assumption to treat hundreds of fibers as one bundle instance. This drastically reduces computational costs compared to direct fiber simulations, while improving disadvantages of approaches based on fiber orientation tensors. Hence, the compression molding process of a full component with thousands of bundles is demonstrated in this contribution. Two-way coupling is achieved using a similar approach to Lindström and Uesaka [23] and results in anisotropic material flow.

2. Direct Bundle Simulation

The fundamental idea of Direct Bundle Simulation is the full description of fiber bundles as a chain of one-dimensional finite elements that experience hydrodynamic drag forces of the surrounding flow. Bundles are represented as truss elements that transfer tensile load, but do not transfer bending torque due to an assumed thread-like nature of the bundle mechanics. Bundle elements may collide with walls or each other. Thus, the direct simulation eliminates the need of empirical interaction parameters in common fiber orientation models such as the Folgar-Tucker constant [10]. Further, this approach allows for the simulation of fiber-matrix separation, as bundles move independently from the matrix material flow.

2.1. Matrix model

The matrix material is subjected to large deformations when it fills the cavity. Thus, the flow of matrix material during molding is described in a Eulerian framework and interacts with the molds through contacts in a Coupled Eulerian-Lagrangian approach [38]. An operator split is utilized to solve the conservation of mass

$$\frac{\partial \rho}{\partial t} + \boldsymbol{\nabla} \cdot (\rho \mathbf{v}) = 0 \tag{4}$$

with mass density ρ and fluid velocity $\mathbf{v}$ as well as the conservation of momentum

$$\frac{\partial \rho \mathbf{v}}{\partial t} + \boldsymbol{\nabla} \cdot (\rho \mathbf{v} \otimes \mathbf{v}) = \boldsymbol{\nabla} \cdot \boldsymbol{\sigma} + \mathbf{f}_{\mathrm{h}} \tag{5}$$

with the stress tensor $\boldsymbol{\sigma}$ and a point-wise body force field imposed by bundles $\mathbf{f}_{\mathrm{h}}$. Such a point-wise body force field was also applied by Lindström et al. [39] to model fiber-fluid coupling.

The conservation equations are split into a Lagrangian step containing only source terms

$$\left.\frac{\partial \rho}{\partial t}\right|_{\mathrm{L}} = 0 \tag{6}$$

$$\left.\frac{\partial \rho \mathbf{v}}{\partial t}\right|_{\mathrm{L}} = \boldsymbol{\nabla} \cdot \boldsymbol{\sigma} + \mathbf{f}_{\mathrm{h}} \tag{7}$$

and a Eulerian step containing the convective terms

$$\left.\frac{\partial \rho}{\partial t}\right|_{\mathrm{E}} + \boldsymbol{\nabla} \cdot (\rho \mathbf{v}) = 0 \tag{8}$$

$$\left.\frac{\partial \rho \mathbf{v}}{\partial t}\right|_{\mathrm{E}} + \boldsymbol{\nabla} \cdot (\rho \mathbf{v} \otimes \mathbf{v}) = \mathbf{0}. \tag{9}$$

The first step is solved analogously to standard Lagrangian procedure on a deforming mesh. In the second step, the deformed mesh is moved back to its original position and the solution variables are updated using a second order advection transport algorithm [40].

The problem is closed with a constitutive model that relates stress to the deformation rate. The stress tensor may be decomposed to a spherical part $\boldsymbol{\sigma}^{\circ}$ and deviatoric part $\boldsymbol{\sigma}'$ according to

$$\boldsymbol{\sigma} = \boldsymbol{\sigma}^{\circ} + \boldsymbol{\sigma}'. \tag{10}$$

Then, the spherical relation is expressed using an equation of state as

$$\boldsymbol{\sigma}^{\circ} = \rho_0 c_0^2 \left(1 - \frac{\rho_0}{\rho}\right) \mathbf{I}, \tag{11}$$

where ρ_0 denotes the mass density of the matrix at rest, c_0 describes the speed of sound, and $\mathbf{I}$ is the second order identity tensor. The deviatoric relation is expressed as isotropic Newtonian viscous behavior

$$\boldsymbol{\sigma}' = \eta \dot{\boldsymbol{\gamma}} \tag{12}$$

with the deviatoric engineering shear strain rate $\dot{\boldsymbol{\gamma}}$ and the dynamic shear viscosity η.

If fiber bundles are neglected, the interaction term $\mathbf{f}_{\mathrm{h}}$ vanishes and the model describes homogeneous isotropic Newtonian flow of the matrix material in the mold. However, fiber bundles move with the flow and the presence of fiber bundles subjects the matrix to an additional force. The determination and application of this contribution to the conservation of momentum is described in the next two sections.

2.2. Hydrodynamic interaction

Stokes' law describes the total hydrodynamic drag force on a sphere with radius $\hat{R}$ as

$$\mathbf{F}_\mathrm{d} = 6\pi\eta\hat{R}\Delta\mathbf{v}, \tag{13}$$

where the relative velocity $\Delta\mathbf{v} = \mathbf{v} - \mathbf{v}_0$ describes the difference between the velocity of the surrounding viscous fluid $\mathbf{v}$ and the velocity of the suspended sphere itself $\mathbf{v}_0$.

For incompressible Newtonian flows with negligible inertia, the absolute hydrodynamic resistance is proportional to $\eta R \left\|\Delta\mathbf{v}\right\|$, independent of the actual shape of a suspended rigid body [41]. Thus, an equivalent radius $\hat{R} = k_\mathrm{d} R$ may be used for shapes different from spheres, where k_d describes a dimensionless correction coefficient and R is a typical linear dimension of the shape, e.g. the cylinder radius. The drag force is always opposing the direction of the relative velocity. Contrary to spheres, cylinders also create lift if they are subjected to a flow with an orientation angle ϕ. Thus, a second analogous coefficient is used to describe lift forces. These lift forces act perpendicular to the relative velocity in direction $\mathbf{q}$ and are computed using a coefficient k_l. In this section, both coefficients are computed for a range of aspect ratios and orientation angles. The coefficients are interpolated using a fitting function that is later used to efficiently compute hydrodynamic forces on bundle segments in the Direct Bundle Simulation.

Multiple cylindrical segments are chained together to represent a bundle, as illustrated in Figure 1. Thus, only forces at the lateral bundle surface A contribute to the total hydrodynamic drag and lift. The ends of the bundle are neglected, as the surface is small compared to the lateral surface. Let $\mathbf{p}$ be the direction of a cylinder positioned at $\mathbf{x}_0 \in \Omega \subset \mathbb{R}^3$, then any point of the cylinder can be described as $\mathbf{r} = r\mathbf{e}_\mathrm{r} + \psi\mathbf{e}_\psi + \zeta\mathbf{p}$, where $\{\mathbf{e}_\mathrm{r}, \mathbf{e}_\psi, \mathbf{p}\}$ describes the local cylinder coordinate system. With this parametrization, the lateral cylinder surface is defined as

$$A := \left\{(r, \psi, \zeta) \in \mathbb{R}^3 \mid r = R, 0 < \psi < 2\pi, 0 < \zeta < L\right\}, \tag{14}$$

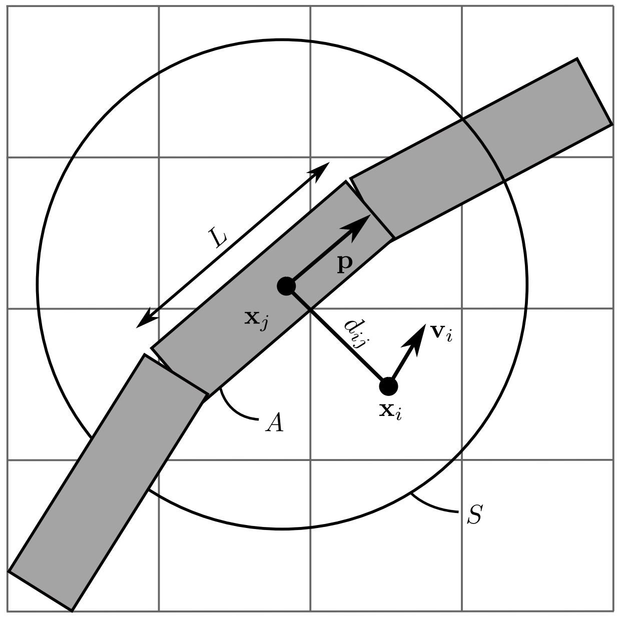

Figure 1: A bundle segment of length L and direction $\mathbf{p}$ is placed in a mesh. The velocity of one exemplary element in the neighborhood S is shown with its current velocity $\mathbf{v}_\mathrm{i}$.

where R is the cylinder radius and L is the length of a bundle segment. The total hydrodynamic force exerted on the cylinder can be determined using an integral over the lateral surface A as

$$\mathbf{F}_\mathrm{h} = \int_A \boldsymbol{\sigma} \cdot \mathbf{n} \, \mathrm{d}A \tag{15}$$

with surface normal $\mathbf{n}$.

To obtain this resistance force for cylinder aspect ratios and orientation angles of interests, a parametric numerical study is performed. A cylinder with radius $R = 0.5\,\mathrm{mm}$ and aspect ratio $r_\mathrm{p} \in \{1, 2, 3, 5, 8, 13, 25\}$ is placed in the center of a cube of fluid Ω with edge length $50\,\mathrm{mm}$. A uniform inlet velocity $v_\infty = 1\,\mathrm{mm\,s^{-1}}$ is applied at x_min and a zero-pressure outlet is applied at x_max. A slip condition with no flux perpendicular to the wall is applied to all other four faces of the cube. At the cylinder surface, a no-slip condition is applied. For each aspect ratio, the orientation angle ϕ, which describes the angle between the velocity direction $\mathbf{v}_\infty = v_\infty \mathbf{e}_\mathrm{x}$ and the cylinder axis $\mathbf{p}$, is varied and a Finite Element Analysis is performed to solve the incompressible steady Stokes flow problem

$$\mathbf{0} = \boldsymbol{\nabla} \cdot \left(-p\mathbf{I} + \eta \left[\boldsymbol{\nabla}\mathbf{v} + (\boldsymbol{\nabla}\mathbf{v})^\top \right] \right) \tag{16}$$

$$\mathbf{0} = \boldsymbol{\nabla} \cdot \mathbf{v}. \tag{17}$$

After computing the velocity field for each configuration, the first and second components of Eq. (15) are used in combination with Eq. (13) to compute the coefficients

$$k_\mathrm{d} = \frac{1}{6\pi\eta R v_\infty} \int_A \boldsymbol{\sigma}_\mathrm{x} \cdot \mathbf{n} \; \mathrm{d}A \tag{18}$$

and

$$k_\mathrm{l} = \frac{1}{6\pi\eta R v_\infty} \int_A \boldsymbol{\sigma}_\mathrm{y} \cdot \mathbf{n} \; \mathrm{d}A \tag{19}$$

from the vertical and horizontal surface stress components $\boldsymbol{\sigma}_\mathrm{x}$ and $\boldsymbol{\sigma}_\mathrm{y}$.

Figure 2 illustrates computed results for different aspect ratios and orientations as points. Additionally, two fits have been determined as

$$k_\mathrm{d}(r_\mathrm{p}, \phi) = 1 - \alpha(r_p - 1)\cos(2\phi) + \beta(r_p - 1) \tag{20}$$

and

$$k_\mathrm{l}(r_\mathrm{p}, \phi) = \alpha(r_p - 1)\sin(2\phi) \tag{21}$$

with $\alpha = 0.09$ and $\beta = 0.3125$.

The fitted Eq. (20) and Eq. (21) are plotted as solid lines in Figure 2. For aspect ratio $r_\mathrm{p} = 1$, the drag is similar to a sphere with $k_\mathrm{d}(1, \phi) \approx 1$ and $k_\mathrm{l}(1, \phi) \approx 0$. For other aspect ratios, the drag increases in a cosine-shape with orientations closer to $\phi = 90°$ and with increasing aspect ratios. The lift force peaks, as expected, at $\phi = 45°$ and follows a sine-shape with an amplitude increasing with the aspect ratio.

Subsequently, it is assumed that micro-scale hydrodynamic effects of the velocity field are included in drag force and lift force. Therefore, bundle segments

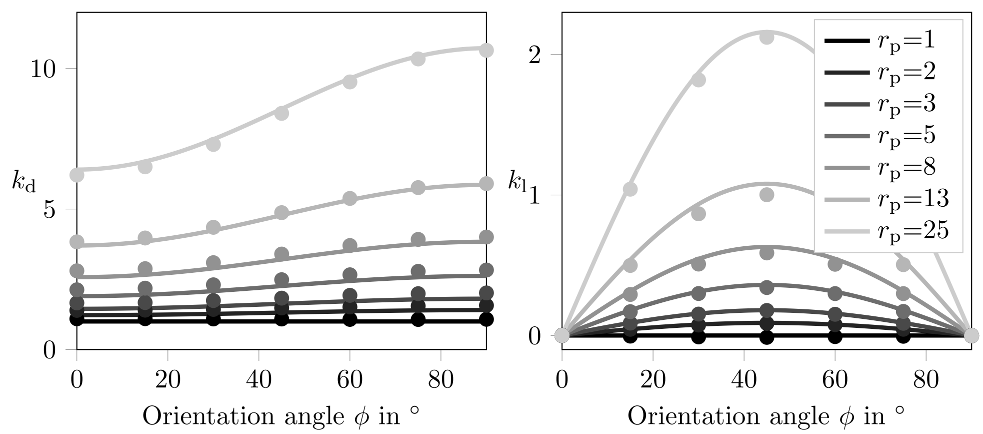

Figure 2: Dimensionless drag coefficient k_d and lift coefficient k_l from computation (dots) and fit according to Eq. (20) and Eq. (21). An orientation angle $\phi = 90°$ means that the cylinder is placed perpendicular to the flow direction and induces maximum drag, while $\phi = 0°$ refers to a cylinder aligned with the velocity $\mathbf{v}_\infty$.

experience only resulting forces and the computation does not need to account for velocity gradients that occur at the subgrid micro-scale.

The surrounding fluid field is computed with a mesh-based approach in this work. Hence, the relative velocity $\Delta\mathbf{v}$ for drag computation has to be determined from nearby matrix elements, as illustrated in Figure 1. The search radius for nearby elements is set to the length of a bundle segment L which leads to the definition of the neighborhood of bundle segment j as $S := \{i \in \mathbb{N} \mid 0 < \|\mathbf{x}_i - \mathbf{x}_j\| < L\}$. Using this neighborhood definition, the relative velocity is computed by a Gaussian weighting approach as

$$\Delta\mathbf{v}_j = \sum_{i \in S} \frac{w_{ij}}{W_j} \left(\mathbf{v}_i - \mathbf{v}_j\right) \tag{22}$$

with Gaussian weighting factors

$$w_{ij} = \exp\left(-\frac{9}{2}\frac{d_{ij}^2}{L^2}\right) \tag{23}$$

and $W_j = \sum_{i \in S} w_{ij}$. The Gaussian weights depend on the distance of a bundle center to a neighboring element d_{ij}. The total hydrodynamic force on a bundle segment j with aspect ratio $r_{\mathrm{p}}^{(j)}$ is computed as

$$\mathbf{F}_{\mathrm{h}}^{(j)} = 6\pi\eta R \left(k_{\mathrm{d}}(r_{\mathrm{p}}^{(j)}, \phi)\Delta\mathbf{v} + k_{\mathrm{l}}(r_{\mathrm{p}}^{(j)}, \phi) \left\| \Delta\mathbf{v} \right\| \mathbf{q} \right) \tag{24}$$

utilizing the orientation angle

$$\phi = \arccos\left(\frac{\Delta\mathbf{v} \cdot \mathbf{p}}{\|\Delta\mathbf{v}\|} \right). \tag{25}$$

The direction of $\mathbf{q}$ is computed from a projection as

$$\mathbf{q} = -\mathrm{sgn}(\mathbf{p} \cdot \Delta\mathbf{v})[\![\mathbf{p} - (\mathbf{p} \cdot [\![\Delta\mathbf{v}]\!])\, [\![\Delta\mathbf{v}]\!]]\!] \tag{26}$$

Here, $\mathbf{p}$ is a unit vector and the operator $[\![\cdot]\!]$ computes a unit vector in the direction of its input and is defined as $[\![\cdot]\!] = (\cdot)/\|\cdot\|$.

After computation of drag forces, the same weights w_{ij} are used to apply an opposing force to each mesh element $i \in S$. The contribution of each bundle j to the coupling body force in element i is expressed as

$$\mathbf{f}_{\mathrm{h}}^{(ij)} = -\frac{1}{V_i}\frac{w_{ij}}{W_j}\mathbf{F}_{\mathrm{h}}^{(j)} \tag{27}$$

with the volume V_i of the i-th element. The total body force field $\mathbf{f}_{\mathrm{h}}$ is then obtained by summing over contributions from all bundles in each element.

2.3. Interaction between fiber bundles

Fiber bundles may collide with mold walls, other bundles or themselves. The collision is treated with a kinematic contact constraint normal to the collision direction utilizing Abaqus' built-in general contact algorithm. All artificial damping parameters are set to zero, because the fluid interaction provides sufficient damping. The tangential friction between fiber bundles is neglected for now, which is a significant simplification. The implication of this simplification is discussed in more detail in Section 5.

2.4. Implementation

The described model is implemented in Abaqus explicit using several subroutines. A VUFIELD subroutine is called at each node to copy node velocities and positions to field variables. The field variables are then interpolated at each integration point by a VUSDFLD subroutine and copied to global arrays. The main task of drag force computation is then treated in a VDLOAD subroutine. Eq. (22) is used to compute the relative velocity at each bundle segment, which is then used to compute drag forces based on Eq. (24) utilizing the coefficients in Eq. (20) and Eq. (21). An opposing force is saved for all neighboring Eulerian elements $i \in S$. Subsequently, Eulerian elements are subjected to a body force field $\mathbf{f}_\mathrm{h}$ computed from the stored drag force and its volume according to Eq. (27).

2.5. Verification

The motion of a single bundle in shear flow is simulated in order to verify the model. The fiber bundle has a length of 25 mm and is subjected to a shear rate $\dot{\gamma} = 10\,\mathrm{s}^{-1}$. The domain for this simulation is

$$\Omega = \left\{\mathbf{x} \in \mathbb{R}^3 \mid -C < (x_2, x_3) < C, -2C < x_1 < 2C\right\} \tag{28}$$

with $C = 20\,\mathrm{mm}$. The bundle is placed at the center, discretized with ten segments and positioned vertically, so that the initial orientation is $\theta = 0$. Figure 3 shows bundle position and velocity in x-direction shortly after starting the simulation. The contour plot of the horizontal velocity component depicted in Figure 3 indicates the two-way coupled nature of the presented approach. Although the bundle is flexible, it behaves like a rigid body until alignment with the flow due to the positive normal stress in the direction of the bundle axis.

A reference solution for this test case is given by Jeffery's equation for a single ellipsoid without buoyancy and inertia [9, 42] in the 2D case as

$$\frac{d\theta}{dt} = \frac{\dot{\gamma}}{2}\left(1 + \xi \cos 2\theta\right). \tag{29}$$

Bretherton [43] showed that this equation is also valid for shapes other than ellipsoids, if an equivalent aspect ratio r_e is used in the shape factor $\xi = (r_\mathrm{e}^2 -$

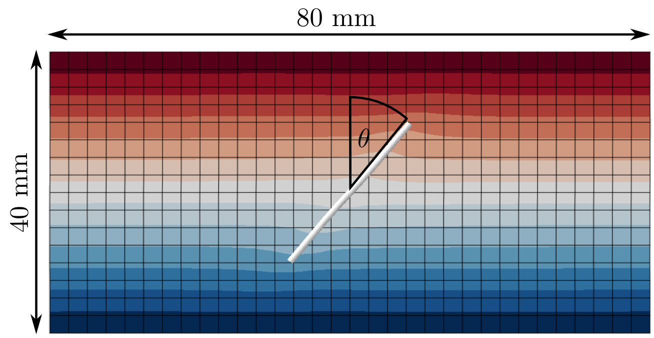

Figure 3: The contour plot shows a fiber bundle discretized with ten segments in a shear flow. The color codes indicate the velocity in x-direction (dark red is $200\,\mathrm{mm\,s^{-1}}$, dark blue is $-200\,\mathrm{mm\,s^{-1}}$). The fluctuations at both ends show how the two-way coupling influences the macroscopic velocity field.

$1)/(r_\mathrm{e}^2 + 1)$. Such equivalent aspect ratios can be determined from the work of Goldsmith and Mason [42] or Cox [44], who suggested the empirical formula

$$r_e = 1.24 \frac{r_\mathrm{p}}{\sqrt{\ln r_\mathrm{p}}} \tag{30}$$

to determine the equivalent aspect ratio r_e from a cylinder aspect ratio r_p.

Figure 4 compares the orientation evolution of the Direct Bundle Simulation with ten truss elements and two truss elements to the solution of Eq. (29). The simulation is in good agreement with the reference solution for both discretizations. Additionally, a bundle with a bundle aspect ratio $r_\mathrm{p} = 25$ is placed 90° to the flow under the same conditions as in the parameter identification (see section 2.2) and meshed with one and ten segments. The resulting drag force normalized with $6\pi\eta R v_\infty$ is 9.31 and 9.55, respectively. This is close to each other, but slightly smaller than the drag coefficient shown in Figure 2, because the averaged velocity around the bundle is smaller than the nominal velocity far away. Anyway, the orientation result and the total drag indicate that bundle motion is generally only slightly affected by discretization. However, the effect on the flow field changes and the approach is not entirely independent of discretization, as one chooses which effects are included in the drag coefficients and which are resolved on the mesh by setting the bundle segment length.

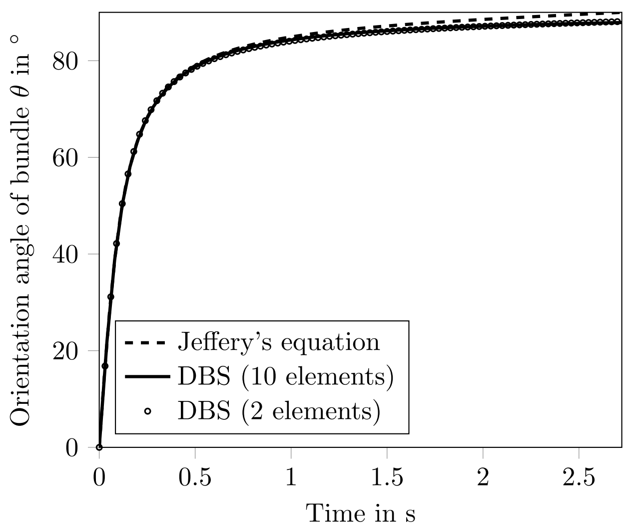

Figure 4: Comparison of bundle orientation angle computed from Direct Bundle Simulation and Jeffery's equation.

There is a small difference between simulation and analytical solution at the almost horizontal state in Figure 4. At this point, torque induced by friction at the lateral surface dominates bundle motion. In SMC, bundles are heavily confined by other bundles and the mold. It is assumed that the torque that spins a free bundle in a dilute situation is small compared to the confinement effects and it is therefore neglected here.

3. Application at component scale

3.1. Molding trials

In this work, a structural SMC based on an UPPH resin system with a composition shown in Table 1 is used. This two-step curing resin was developed to improve co-molding with unidirectional carbon fiber patches due to a higher viscosity in the B-stage [45].

The specimen under investigation is a hat profile with outer dimensions 120 mm x 94 mm and a final thickness of 2 mm. Two variants are molded: Variant

Table 1: Composition of UPPH Sheet Molding Compound

Component	**Trade name**	**Quantity**
UPPH resin	Daron ZW 14141	100 parts
Flow aid	BYK 9085	2 parts
Impregnation aid	BYK 9076	3 parts
Deaeration aid	BYK A-530	0.5 parts
Inhibitor	pBQ	0.3 parts
Peroxide	Trignox 117	1 part
Isocyanate	Lupranat M20R	24.2 parts
Glass fiber	Multistar 272 4800 80	23 vol%

"S" (split configuration) consists of two SMC stacks ("S1" and "S2") with dimensions 80 mm x 30 mm x 5.3 mm that are manually placed in the mold as illustrated in Figure 5 with dotted outlines. This split stack allows the investigation of weld line formation during the flow. The second variant "A" uses an asymmetric placement of a single stack with dimensions 80 mm x 60 mm x 5.3 mm and enables a longer flow path. The mold is heated to 145 °C and closed with a hydraulic press. The maximum press force was limited to 50 kN.

3.2. CT Analysis

The molded samples were analyzed by volumetric imaging using an Yxlon X-ray CT system with a Perkin Elmer flat panel Y.XRD1620 detector and a reflection tube by Comet. The detector has a resolution of 2048×2048 pixels and a pixel pitch of 200 µm. Acceleration voltage, current, exposure time and frame binning were set to 150 kV, 0.05 mA, 1000 ms and 2, respectively. A 16-bit volumetric image gray scale image is reconstructed based on 2400 projections over 360° and the Feldkamp, Davis and Kress (FDK) algorithm [46]. The voxel size of the resulting volumetric image is 68.7 µm.

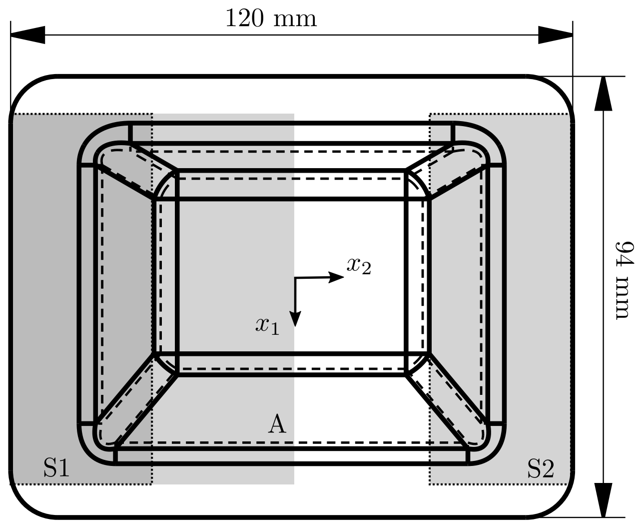

Figure 5: The molded part has outer dimensions 120 mm x 94 mm. For the split stack configuration, two SMC stacks "S1" and "S2" are placed at the light gray areas with dotted outlines. For the asymmetric configuration, a single stack ("A") is placed on one side of the mold.

3.3. Compression Molding Simulation

The molding process is simulated using Abaqus explicit utilizing the Coupled Lagrangian Eulerian (CEL) feature. In this method, operator splitting is applied to divide the momentum equation in a Langrangian step and a subsequent Eulerian step for material transport, as explained in Section 2.1. The fluid phase is represented by an element-wise material volume fraction and an immersive boundary is reconstructed at each step for interactions with the molds [38]. Fiber bundles interact with the SMC phase exclusively through the subroutines described in Section 2.4.

The total part volume is 25 410 mm^3, which leads to a bundle volume of 5844 mm^3 at the given nominal fiber volume fraction. The roving used for SMC production is a 4800 Tex multi-end roving with 80 strands and fiber diameter of 14 µm. Hence, each bundle is comprised of approximately 200 fibers, which leads to a total amount of 7600 bundles with 25 mm length in the part. The initial microstructure for the simulation is generated by sampling bundle directions randomly from a uniform planar-isotropic fiber orientation distribution. The bundles are then randomly shifted such that at least one node remains in the stack volume. This way, a statistically uniform fiber volume fraction is achieved in the stack region. Each bundle is discretized with ten linear truss elements and all elements outside the stack are cut, similar to the physical process, in which the stack is cut from an SMC sheet.

Additionally, Eulerian elements are used to represent the molding domain. Only those Eulerian elements occupied by initial stack positions are initially filled with material. Both mold halfs are represented by rigid shell elements. They interact with the SMC paste through hydrodynamic friction

$$\boldsymbol{\tau} = -\lambda \left(\frac{\|\mathbf{v}_{\mathrm{rel}}\|}{v_0} \right)^{m-1} \mathbf{v}_{\mathrm{rel}} \tag{31}$$

with a friction coefficient λ, a reference velocity v_0, a power law coefficient m and the relative velocity in the contact plane $\mathbf{v}_{\mathrm{rel}}$. This formulation is quite common and physically motivated by a resin-rich lubrication layer near the hot mold [6, 47]. Parameters are estimated from a similar material system [48] and listed in Table 2.

The explicit time integration requires an extremely small time increment due to the high resin viscosity. The mass of the entire model was therefore scaled by a factor κ_{m} to improve the time increment, while ensuring that kinetic energy remains negligible small compared to the external work. The viscosity dominated time step scales linearly with density. Additional simulation parameters are listed in Table 2.

While the lower mold is constrained at a fixed position, the upper mold is closed with the profiles given in Figure 6. These profiles are an idealization to save computational time during the initial forming process, before the flow of material starts. There is some variation in the experimental profiles, which can be attributed partly to a non-uniform thickness of SMC sheets and to the reaction time of the press control unit. The simulation stops after a complete fill with the final part height and does not include the subsequent holding and

Table 2: Simulation Parameters

Property	**Symbol**	**Value**
Resin viscosity	η	1×10^5 Pa s
Resin mass density	ρ_r	$1900\,\mathrm{kg\,m^{-3}}$
Resin speed of sound	c_0	$1000\,\mathrm{m\,s^{-1}}$
Bundle elastic modulus	E	73 GPa
Bundle density	ρ_b	$2600\,\mathrm{kg\,m^{-3}}$
Bundle radius	R	0.1 mm
Bundle segment length	L	2.5 mm
Mold friction coefficient	λ	$1 \times 10^6\,\mathrm{N\,s\,m^{-3}}$
Mold friction exponent	m	0.6
Reference velocity	v_0	$0.001\,\mathrm{m\,s^{-1}}$
Mass scaling factor	κ_m	1×10^6
Time step	Δt	3×10^{-4} s

curing process. The computational time for the simulation is approximately 22 hours on a single workstation with a Intel Xeon E5 2667V2 CPU.

A conventional simulation utilizing fiber orientation tensors and Jeffery's equation is used to compare the Direct Bundle Simulation to the macroscopic orientation model given in Eq. (3). A VUMAT subroutine with six state variables and an IBOF closure approach [49] for the fourth order fiber orientation tensor $\mathbb{A}$ was implemented to compute fiber orientations instead of the bundle motion. In this conventional approach, no two-way coupling was included. The initial fiber orientation is described by a planar isotropic fiber orientation tensor and all other conditions remain unchanged.

4. Results

Figure 7 provides an overview on the compression molding process simulation for the split stack configuration "S". The initial mold gap at $t = 0$ s is 20 mm

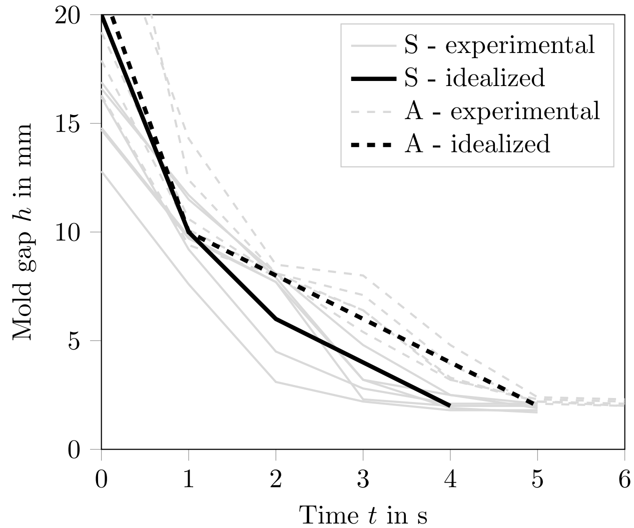

Figure 6: Distance between upper and lower mold during the flowing phase of SMC. Six parts of the split configuration "S" were produced and are shown with solid gray lines. Four parts of the asymmetric configuration "A" were produced and are shown with dashed gray lines. Additionally, the idealized mold profiles for simulations are shown in solid black and dashed black for the "S" and "A" configuration, respectively.

and the upper mold is just not touching the SMC stacks. Closing the mold with the high initial closing speed deforms the stacks, but does not start material flow. During forming, the two-way coupled approach pulls the stack sideways in the hat-shaped mold. This can be observed by the lateral deformation of the stack tips depicted at $t = 2\,\mathrm{s}$ in Figure 7. The mold gap is reduced to the initial stack height of 5.3 mm after approximately two seconds. From there on, flow dominates the mold filling process and fiber bundles are carried with the SMC until the final part thickness of 2 mm is reached.

4.1. Orientation and separation effects

Figure 8 shows slices through the midplane of the upper and lower planar regions of the scanned part in split stack configuration. Additional slices through thickness are provided in Figure A.14 in the appendix. The white strands represent fiber bundles, which remain in their bundled structure even for the applied

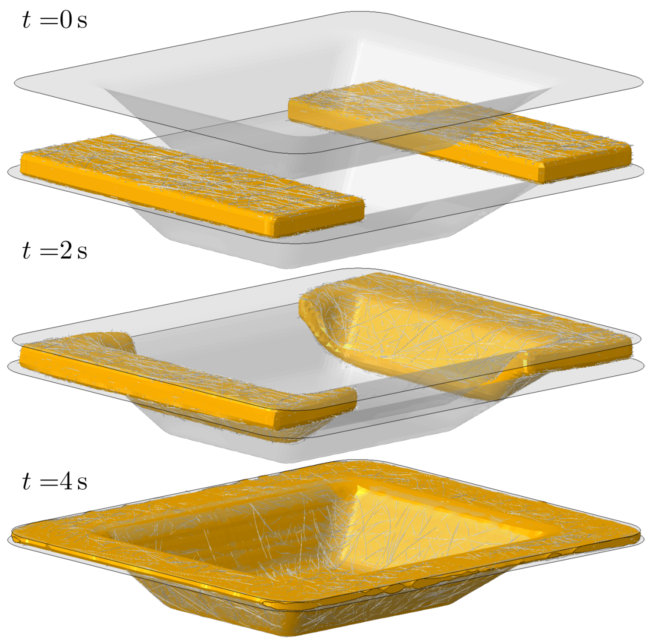

Figure 7: Snapshots of the molding process for the split stack configuration "S". The compression molding process starts with a deformation of the two initial stacks. Subsequently, the SMC is forced to flow until the part reaches its final thickness of 2 mm. The Direct Bundle Simulation approach lets bundles deform and flow with the matrix material while enforcing two-way coupling. Therefore, the flow is naturally anisotropic and depends on the current bundle configuration.

high degree of deformation. The weld line features a severe fiber-matrix separation and only a small amount of fiber bundles bridges the gap in this zone. The inner slice in Figure 8 even shows some pores. Regions close to the mold boundaries and the weld line show a bundle alignment parallel to the boundary. Bundles perpendicular to the boundary are likely pulled out of this region by forces acting over the entire length of the bundle and parallel bundles remain close to the boundaries. Regions farther away from boundaries show a regular random in-plane orientation.

The Direct Bundle Simulation result is sliced in the same planes and the result is depicted in Figure 9. The simulation results show a slightly larger area of

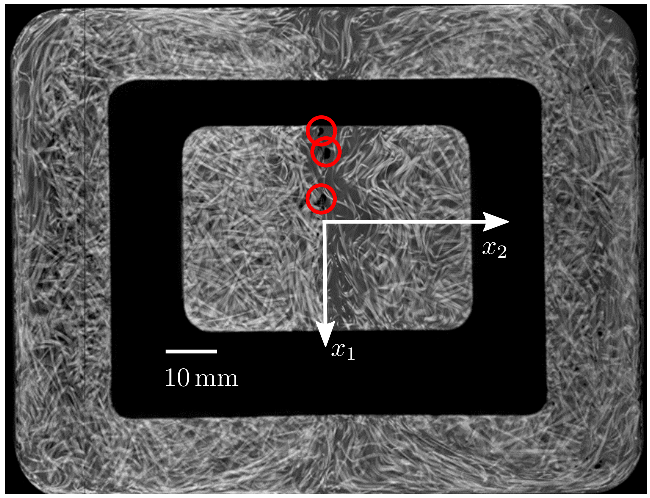

Figure 8: Slices through the upper and lower planar regions of the CT Scan.Fiber bundles stay intact during molding and fiber-matrix separation can be observed at the weld line. The weld line region includes pores (marked with red circles) close to the origin of the coordinate system.

fiber-matrix separation and no bundles bridge the resin-rich weld line. Similar to the CT-scan, boundary regions show a predominant orientation parallel to the boundaries.

For a quantitative comparison of the Direct Bundle Simulation to a simulation based on fiber orientation tensors and the CT scans, bundle orientations are evaluated on a uniform 12 x 16 x 4 grid of sub-volumes. The discrete second-order fiber orientation tensor for each of the sub-volumes is computed as

$$\mathbf{A} = \frac{1}{N}\sum_{i=1}^{N} \mathbf{p}_{\mathrm{i}} \otimes \mathbf{p}_{\mathrm{i}} \tag{32}$$

with N being the number of truss elements in the sub-volume.

The slices of the CT scan shown in Figure 8 are analyzed in 2D using OrientationJ [50], such that a major direction is assigned to each 10x10 pixel area. Then the same discrete fiber orientation tensor definition given in Eq. (32) and the same 12 x 16 grid is used to represent the orientation state as tensor components.

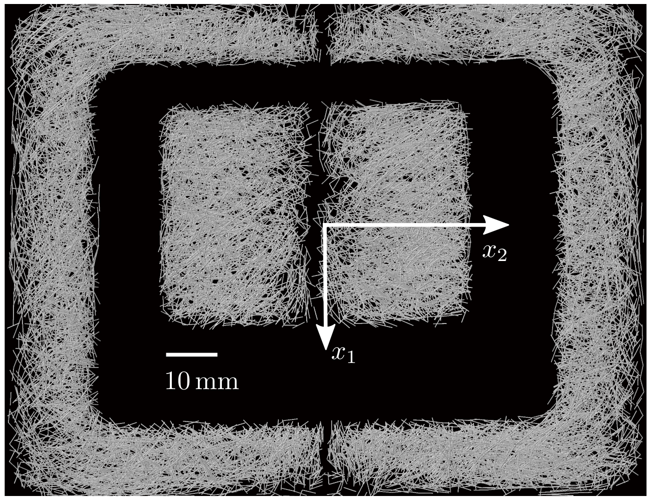

Figure 9: Slices through the planar regions of the Direct Bundle Simulation result. Each gray cylinder represents a bundle segment consisting of 200 individual fibers. The weld line at the center is matrix rich and no bundles gap the this region. Bundles close to the boundaries show a reduced fiber volume fraction and more bundles oriented parallel to the boundary.

A comparison of the Direct Bundle Simulation approach, CT scan and the conventional fiber orientation model is depicted in Figure 10 for the split stack configuration. The A_{11}-component of the CT-analysis features three significantly higher oriented vertical stripes at both ends of the mold and the weld line. Conversely, the A_{22}-component of the CT-analysis indicates a dominant orientation in horizontal direction at the top and bottom mold boundaries with lower values at the vertical mold boundaries to the left and right of the figure. The corresponding Direct Bundle Simulation is able to reproduce these three stripes of higher vertical orientation at the correct positions. Characteristic gradients and the level of orientation is predicted well. The conventional approach using fiber orientation tensors and Jeffery's equation does not account for the constraints at mold walls and shows a homogeneous orientation distribution. In homogeneous regions, such as the inner slice with some distance to the weld line, Jeffery's equation leads to a reasonable prediction of the orientation state.

The Direct Bundle Simulation limits any bundle orientation normal to the

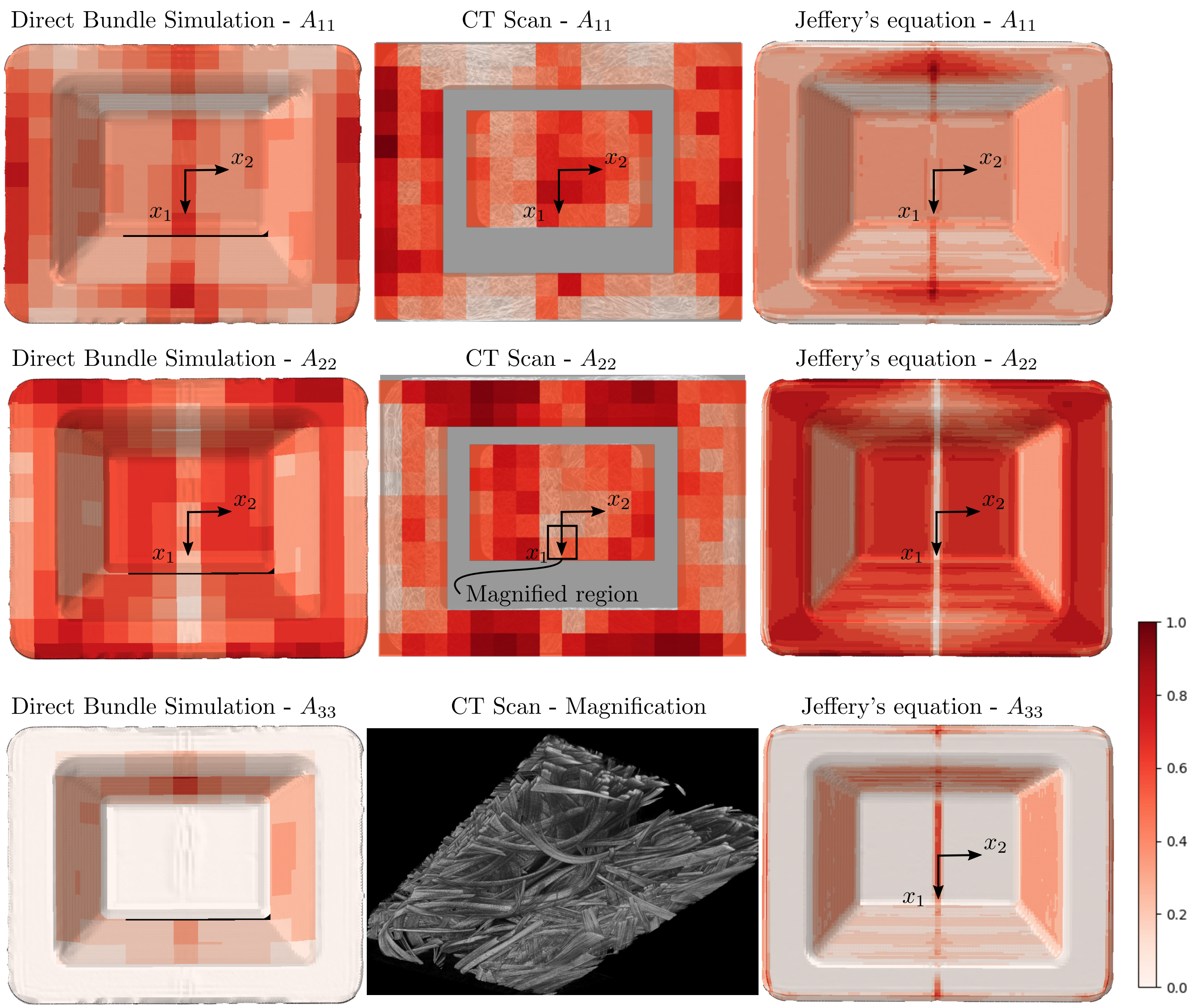

Figure 10: Comparison of Direct Bundle Simulation results with CT Analysis and fiber orientation tensor based computation utilizing Jeffery's equation for the split stack configuration. The first row shows orientation tensor component A_{11} which indicates vertical fiber orientation in this representation. The second row shows the A_{22}-component representing horizontal fiber orientation. The third row shows the A_{33}-component representing fiber orientation normal to the observation plane. The orientation analysis of the CT image slices is limited to two dimensions. Thus, the central image in the third row shows a high resolution CT scan of the region indicated in the illustration above. The magnified view reveals a dominant in-plane orientation of bundles.

molds, because bundle segments cannot be physically arranged in normal direction in the constrained mold gap. Thus, the A_{33}-component is small in the planar regions of the part. An investigation of a magnified CT Scan with higher resolution confirms that fiber bundles at the weld line are primarily oriented in-plane. The computation based on fiber orientation tensors shows a dominant normal component of fiber orientation at the weld line.

Figure 11 is analogous to Figure 10, but describes the evaluation of the asymmetric stack configuration with a maximum flow path of 60 mm in x_2-direction. This configuration confirms observations of the previous case with significantly higher orientations parallel to mold walls that are not described by tensor based theory. Despite a longer flow path, the magnitude of re-orientation is similar to the split stack configuration due to a similar stretch in x_2-direction (50% initial mold coverage each).

4.2. Bundle curvature

The curvature of bundles is evaluated as

$$\kappa = \frac{2}{L} \tan\left(\frac{1}{2} \arccos\left(\llbracket \mathbf{p}^{(j)} \rrbracket \cdot \llbracket \mathbf{p}^{(k)} \rrbracket\right)\right) \tag{33}$$

at each node connecting two neighboring bundles j and k. A contour plot of the curvature for the split stack configuration is plotted in Figure 12. It shows that the largest curvatures occur at corners and close to the weld line. The curvature at the weld line originates probably from a flow in x_1 direction compressing bundles to a zig-zag shape. The curvature in the CT scan is obtained only for the central region in order to have sufficient resolution for tracking bundle curvature [51].

The projection of curvature values on the x_1 direction is plotted in Figure 13. The maximal values of the CT scan agree well with the maximal curvatures computed from the direct bundle simulation. The mean curvature of the CT scan is higher in this representation, but this is likely influenced by the lower values outside the center region which are not taken into account for the CT

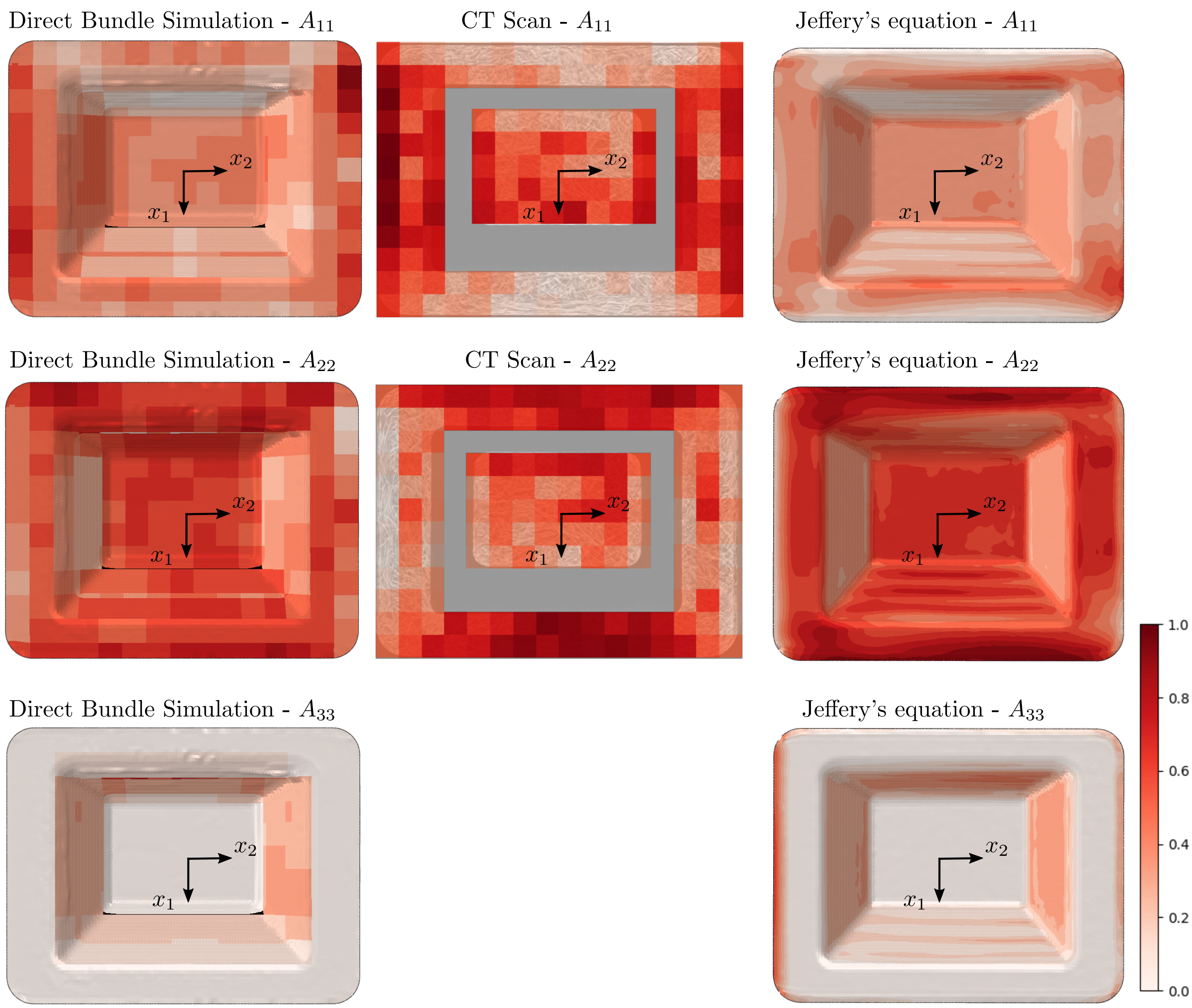

Figure 11: Comparison of Direct Bundle Simulation results with CT Analysis and fiber orientation tensor based computation utilizing Jeffery's equation for the asymmetric stack configuration. Refer to Figure 10 for a detailed explanation of the layout.

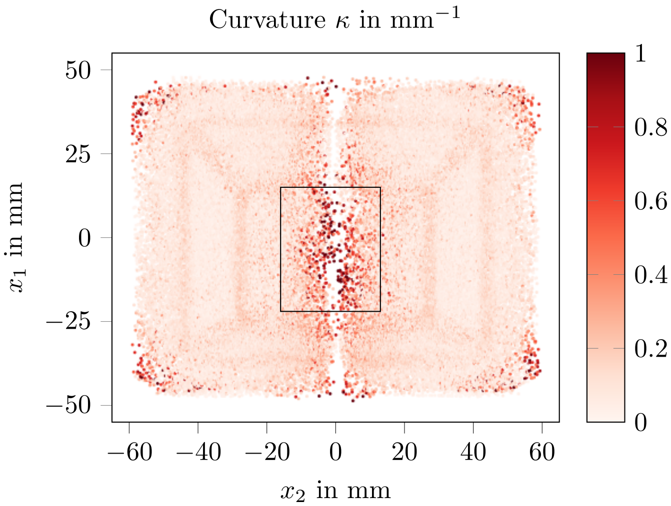

Figure 12: Simulation results of bundle curvature. The highest values occur at the corners of the mold and at the weld line. The parts three dimensional shape is visible in this plot due to the bending of bundles at curvatures of the geometry. High resolution CT data for curvatures is obtained for the central area marked with a black rectangle.

data. It should be mentioned that simulated curvature might depend on the segment length of bundles.

5. Discussion

5.1. Simplifications and Limitations

The entire flow of material is assumed to be isothermal in this work. This assumption is quite common for the bulk material of SMC, as the time scale of thermal diffusivity in SMC is large compared to the time it takes the material to flow (less than 5 s). Consequently, curing during the flow is also neglected. The heating and curing of bulk material is a relevant process in the subsequent holding phase though, which takes approximately 2 min.

The matrix is treated as a purely viscous Newtonian fluid, because shear thinning behavior of the matrix system is currently not available. Typically, SMC matrix is described with a non-Newtonian power law model [6, 7, 52], which

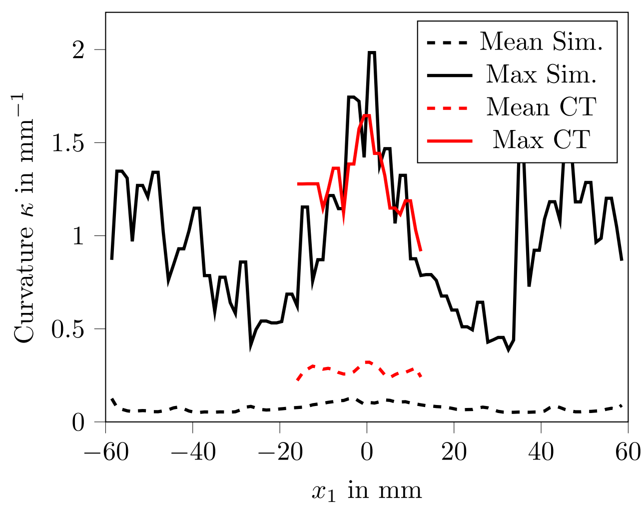

Figure 13: Curvatures projected to the x_2 axis.

has certainly an influence on the necessary compression force. However, the method is by no means limited to Newtonian viscosity. The characterization can be performed in a standard rheometer without fibers and does not require complex in-mold measurements.

Fiber bundles are represented with truss elements which neglect bending stiffness and transfer tension only. This is based on the assumption that bundles have much higher bending compliance compared to a homogeneous cylinder. Bending and tension are likely decoupled at the meso-scale, as individual filaments may slide in relative motion. However, modeling the complex mechanics of a bundle and its sizing as a truss is a simplification in the present model. Truss elements imply a cylindrical shape for collisions in the current implementation. This is a simplification, because bundles in the actual process are mostly flat. Further work is required to investigate the effect of bundle shape on resulting micro structures. Additionally, short range hydrodynamic interactions (lubrication forces) between bundles are neglected. These interaction forces occur if bundles come in close contact and matrix material is sheared in the small gap between them.

An a priori estimate for the number of contacts per bundle segment is given as

$$N_{\mathrm{c}} = 4f\left(\frac{2}{\pi}\frac{L}{2R}\Phi_1 + \Phi_2 + 1\right) \tag{34}$$

with the orientation functions $\Phi_1 = \Phi_2 = 2/\pi$ for a 2D random fiber distribution and volume fraction f [53]. This estimate predicts about 6.2 contacts per bundle segment, which makes the incorporation of short-range hydrodynamics necessary for the correct prediction of compression forces. An evaluation of the direct bundle simulation leads to an average of 4.6 to 5.0 contacts per bundle (see appendix Appendix B). This evaluation is in good agreement with the estimate given in equation (34). An additional challenge in modeling lubrication is the increasing sheared area due to flattening bundles [35]. The introduction of lubrication effects and corresponding experimental investigations with pressure sensors will be addressed by the authors in future work.

5.2. Comparison of Direct Bundle Simulation to the State of the Art

The Direct Bundle Simulation is able to predict fiber-matrix separation effects at the weld line and thus enables a better description of structural weak spots in such areas. The simulated matrix-rich region is slightly larger than in the investigated sample. This might be caused either by the experimental setup, because the part was compressed further than the nominal thickness, or by the simplifications of the model (bundle shape and friction).

The presented approach is a natural access to modeling anisotropic flow. Other simulations based on fiber orientation tensors may incorporate the fourth order fiber orientation tensor to describe the fourth order viscosity tensor. However, the fourth order orientation tensor must be approximated by a closure, which becomes increasingly inaccurate, if only a few bundled directions are dominant.

At regions close to the mold walls and the weld line, Direct Bundle Simulation accounts for spatial constraints of the fiber orientation due to mold boundaries and leads to more accurate fiber orientation results. This is expected to be useful for narrow features such as ribs or beads. Nonetheless, Jeffery's equation leads to reasonable results in planar, homogeneous regions and has an approximately ten times faster computational time. Therefore, a hybrid approach with bundles in critical regions might be a solution to improve computational efficiency for large SMC parts.

Finally, simulation and experiment represent only single realizations of random processes. The ability to run multiple simulations with different initial microstructures may help estimating process reliability and statistical deviations in future.

6. Conclusion

The Direct Bundle Simulation approach treats fiber bundles in SMC as one-dimensional instances that move independent of the matrix material and interact through hydrodynamic forces as well as contact forces. The computational effort is greatly reduced compared to a simulation of all fibers by utilizing the observation that most bundles stay in a bundled configuration during SMC compression molding. The approach reproduces Jeffery's equation for a single fiber bundle in shear flow. A part with double-curved geometry was molded using two initial charges in order to force formation of a weld line and with a single initial charge to provide a long flow path. CT analysis of the parts shows that the Direct Bundle Simulation is able to predict a resin rich weld line and accounts for long fiber orientation constraints. Predicting such manufacturing defects in SMC compression molding enables the optimization of process parameters and molds early in the development process.

Compared to statistical descriptors of fiber orientation, such as commonly used second order fiber orientation tensors, the direct simulation approach offers several advantages: Regions, where fiber lengths are comparable to local dimensions of the mold and thus where scale separation does not apply, can be described. This leads to an improved accuracy of computed fiber orientation data at weld lines and close to the mold boundaries. The distribution of fiber volume fraction and fiber-matrix separation effects can be simulated, as bundles move independent of the matrix material. Flow anisotropy is treated naturally by imposing opposing forces to the fluid phase and does not rely on a closure approximation of the fourth order fiber orientation tensor. Additionally, the number of contacts and bundle curvature can be computed and shows good agreement with analytical estimates or evaluation of CT data.

Acknowledgments

The research documented in this manuscript has been funded by the German Research Foundation (DFG) within the International Research Training Group "Integrated engineering of continuous-discontinuous long fiber-reinforced polymer structures" (GRK 2078). The support by the German Research Foundation (DFG) is gratefully acknowledged.

Contributions

NM developed and implemented the Direct Bundle Simulation approach and wrote the first draft of the manuscript. LS performed CT scans and reconstructed the 3D images. LB suggested the mold configuration and performed molding trials together with NM. AH supervised the work in terms of composite process knowledge and relevance of the addressed subjects. LK suggested to include two-way coupling in the Direct Bundle Simulation and supervised the presented work.

Conflict of interest

We wish to confirm that there are no known conflicts of interest associated with this publication and there has been no significant financial support for this work that could have influenced its outcome.

Appendix A. Slices through thickness

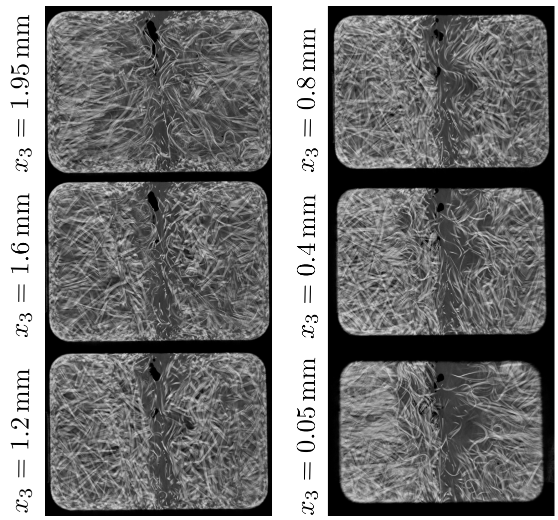

Figure A.14: Equidistant slices through the center area of the CT scan. Bundles are spread close to the mold walls, which can be seen as blurry distribution at $x_3 = 0.05\,\mathrm{mm}$ and $x_3 = 1.95\,\mathrm{mm}$ at this resolution. Most bundles in the core stay intact. There is no other pronounced difference between core and shell, which is in agreement with the plug-flow assumption for SMC [3].

Appendix B. Contacts

The total number of contacts is evaluated for each frame of the simulation results and is plotted in Figure B.15. This averages to approximately 1.8×10^5 contact *pairs* for the split stack configuration and 2.2×10^5 contact *pairs* for the asymmetric flow, which has a slightly increased fiber volume fraction compared to the nominal value. Considering the total amount of 77438 and 87950 bundle segments, this evaluates to 4.6 and 5.0 contacts per bundle segment, respectively.

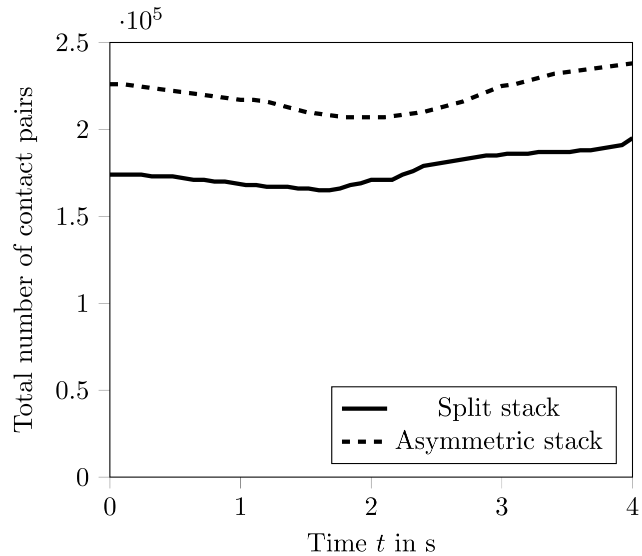

Figure B.15: Number of bundle-bundle contacts pairs during the molding process. The number of contact pairs decreases during the forming phase of the stack and increases during flow, when the entire stack is compressed.

References

[1] J. Görthofer, N. Meyer, T. D. Pallicity, L. Schöttl, A. Trauth, M. Schemmann, M. Hohberg, P. Pinter, P. Elsner, F. Henning, A. N. Hrymak, T. Seelig, K. Weidenmann, L. Kärger, T. Böhlke, Virtual process chain of sheet molding compound: Development, validation and perspectives, Composites Part B: Engineering 169 (2019) 133–147. doi:10.1016/j.compositesb.2019.04.001.

[2] R. J. Silva-Nieto, B. C. Fisher, A. W. Birley, Predicting mold flow for unsaturated polyester resin sheet molding compounds, Polymer Composites 1 (1) (1980) 14–23. doi:10.1002/pc.750010105.

[3] M. R. Barone, D. A. Caulk, A model for the flow of a chopped fiber reinforced polymer compound in compression molding, Journal of Applied Mechanics 53 (1986).

[4] M. R. Barone, T. A. Osswald, A boundary element analysis of flow in sheet molding compound, Polymer Composites 9 (2) (1988) 158–164. doi:10.1002/pc.750090210.

[5] L. M. Abrams, J. M. Castro, Predicting molding forces during sheet molding compound (smc) compression molding. i: Model development, Polymer Composites 24 (3) (2003) 291–303. doi:10.1002/pc.10029.

[6] P. Dumont, L. Orgéas, D. Favier, P. Pizette, C. Venet, Compression moulding of smc: In situ experiments, modelling and simulation, Composites Part A: Applied Science and

Manufacturing 38 (2) (2007) 353–368. doi:10.1016/j.compositesa.2006.03.010.

[7] M. Hohberg, L. Kärger, F. Henning, A. Hrymak, Rheological measurements and rheological shell model considering the compressible behavior of long fiber reinforced sheet molding compound (SMC), Composites Part A: Applied Science and Manufacturing 95 (2017) 110–117. doi:10.1016/j.compositesa.2017.01.006.

[8] S. G. Advani, C. L. Tucker, The use of tensors to describe and predict fiber orientation in short fiber composites, Journal of Rheology 31 (8) (1987) 751–784. doi:10.1122/1.549945.

[9] G. B. Jeffery, The motion of ellipsoidal particles immersed in a viscous fluid, Proceedings of the Royal Society of London. Series A 102 (715) (1922) 161–179. doi:10.1098/rspa.1922.0078.

[10] F. Folgar, C. L. Tucker, Orientation behavior of fibers in concentrated suspensions, Journal of Reinforced Plastics and Composites 3 (2) (1984) 98–119. doi:10.1177/073168448400300201.

[11] J. Wang, J. F. O'Gara, C. L. Tucker, An objective model for slow orientation kinetics in concentrated fiber suspensions: Theory and rheological evidence, Journal of Rheology 52 (5) (2008) 1179–1200. doi:10.1122/1.2946437.

[12] J. H. Phelps, C. L. Tucker, An anisotropic rotary diffusion model for fiber orientation in short- and long-fiber thermoplastics, Journal of Non-Newtonian Fluid Mechanics 156 (3) (2009) 165–176. doi:10.1016/j.jnnfm.2008.08.002.

[13] E. J. Hinch, The distortion of a flexible inextensible thread in a shearing flow, Journal of Fluid Mechanics 74 (2) (1976) 317–333. doi:10.1017/S002211207600181X.

[14] S. Yamamoto, T. Matsuoka, A method for dynamic simulation of rigid and flexible fibers in a flow field, The Journal of Chemical Physics 98 (1) (1993) 644–650. doi:10.1063/1.464607.

[15] P. Skjetne, R. F. Ross, D. J. Klingenberg, Simulation of single fiber dynamics, The Journal of Chemical Physics 107 (6) (1997) 2108–2121. doi:10.1063/1.474561.

[16] N. Phan-Thien, X. J. Fan, R. I. Tanner, R. Zheng, Folgar-Tucker constant for a fibre suspension in a Newtonian fluid, Journal of Non-Newtonian Fluid Mechanics 103 (2-3) (2002) 251–260. doi:10.1016/S0377-0257(02)00006-X.

[17] R. F. Ross, D. J. Klingenberg, Dynamic simulation of flexible fibers composed of linked rigid bodies, The Journal of Chemical Physics 106 (7) (1997) 2949–2960. doi:10.1063/1.473067.

[18] G. Meirson, A. N. Hrymak, Two-dimensional long-flexible fiber simulation in simple shear flow, Polymer Composites 37 (8) (2016) 2425–2433. doi:10.1002/pc.23427.

[19] Y. Yamane, Y. Kaneda, M. Dio, Numerical simulation of semi-dilute suspensions of rodlike particles in shear flow, Journal of Non-Newtonian Fluid Mechanics 54 (1994) 405–421. doi:10.1016/0377-0257(94)80033-2.

[20] R. R. Sundararajakumar, D. L. Koch, Structure and properties of sheared fiber suspen-

sions with mechanical contacts, Journal of Non-Newtonian Fluid Mechanics 73 (3) (1997) 205–239. doi:10.1016/S0377-0257(97)00043-8.

[21] X. J. Fan, N. Phan-Thien, R. Zheng, A direct simulation of fibre suspensions, Journal of Non-Newtonian Fluid Mechanics 74 (1-3) (1998) 113–135. doi:10.1016/S0377-0257(97)00050-5.

[22] G. Ausias, X. J. Fan, R. I. Tanner, Direct simulation for concentrated fibre suspensions in transient and steady state shear flows, Journal of Non-Newtonian Fluid Mechanics 135 (1) (2006) 46–57. doi:10.1016/j.jnnfm.2005.12.009.

[23] S. B. Lindström, T. Uesaka, Simulation of the motion of flexible fibers in viscous fluid flow, Physics of Fluids 19 (11) (2007) 113307. doi:10.1063/1.2778937.

[24] S. B. Lindström, T. Uesaka, A numerical investigation of the rheology of sheared fiber suspensions, Journal of Fluid Mechanics 21 (8) (2009) 083301. doi:10.1063/1.3195456.

[25] D. Kunhappan, B. Harthong, B. Chareyre, G. Balarac, P. J. J. Dumont, Numerical modeling of high aspect ratio flexible fibers in inertial flows, Physics of Fluids 29 (9) (2017) 093302. doi:10.1063/1.5001514.

[26] C. F. Schmid, L. H. Switzer, D. J. Klingenberg, Simulations of fiber flocculation: Effects of fiber properties and interfiber friction, Journal of Rheology 44 (4) (2000) 781–809. doi:10.1122/1.551116.

[27] R. Mezher, E. Abisset-Chavanne, J. Férec, G. Ausias, F. Chinesta, Direct simulation of concentrated fiber suspensions subjected to bending effects, Modelling and Simulation in Materials Science and Engineering 23 (5) (2015) 055007. doi:10.1088/0965-0393/23/5/055007.

[28] A. I. Abd El-Rahman, C. L. Tucker, Mechanics of random discontinuous long-fiber thermoplastics. part ii: Direct simulation of uniaxial compression, Journal of Rheology 57 (5) (2013) 1463–1489. doi:10.1122/1.4818804.

[29] S. Le Corre, D. Caillerie, L. Orgéas, D. Favier, Behavior of a net of fibers linked by viscous interactions: theory and mechanical properties, Journal of the Mechanics and Physics of Solids 52 (2) (2004) 395–421. doi:10.1016/S0022-5096(03)00090-5.

[30] S. Le Corre, P. Dumont, L. Orgéas, D. Favier, Rheology of highly concentrated planar fiber suspensions, Journal of Rheology 49 (5) (2005) 1029–1058. doi:10.1122/1.1993594.

[31] P. Dumont, S. Le Corre, L. Orgéas, D. Favier, A numerical analysis of the evolution of bundle orientation in concentrated fibre-bundle suspensions, Journal of Non-Newtonian Fluid Mechanics 160 (2-3) (2009) 76–92. doi:10.1016/j.jnnfm.2009.03.001.

[32] C. Kuhn, I. Walter, O. Täger, T. A. Osswald, Simulative prediction of fiber-matrix separation in rib filling during compression molding using a direct fiber simulation, Journal of Composites Science 2 (1) (2017) 2. doi:10.3390/jcs2010002.

[33] S. Hayashi, H. Chen, W. Hu, Development of new simulation technology for compression molding of long fiber reinforced plastics, The Proceedings of The Computational

Mechanics Conference 2017.30 (0) (2017) 012. doi:10.1299/jsmecmd.2017.30.012.

[34] P. Dumont, J.-P. Vassal, L. Orgéas, V. Michaud, D. Favier, J.-A. E. Månson, Processing, characterisation and rheology of transparent concentrated fibre-bundle suspensions, Rheologica Acta 46 (5) (2007) 639–651. doi:10.1007/s00397-006-0153-8.

[35] T.-H. Le, P. Dumont, L. Orgéas, D. Favier, L. Salvo, E. Boller, X-ray phase contrast microtomography for the analysis of the fibrous microstructure of smc composites, Composites Part A: Applied Science and Manufacturing 39 (1) (2008) 91–103. doi:10.1016/j.compositesa.2007.08.027.

[36] O. Guiraud, L. Orgéas, P. J. J. Dumont, S. Du Rolland Roscoat, Microstructure and deformation micromechanisms of concentrated fiber bundle suspensions: An analysis combining x-ray microtomography and pull-out tests, Journal of Rheology 56 (3) (2012) 593–623. doi:10.1122/1.3698185.

[37] A. Motaghi, A. N. Hrymak, Microstructure characterization in direct sheet molding compound, Polymer Composites 40 (S1) (2019) E69–E77. doi:10.1002/pc.24495.

[38] D. J. Benson, S. Okazawa, Contact in a multi-material eulerian finite element formulation, Computer Methods in Applied Mechanics and Engineering 193 (39-41) (2004) 4277–4298. doi:10.1016/j.cma.2003.12.061.

[39] S. B. Lindström, T. Uesaka, Simulation of semidilute suspensions of non-brownian fibers in shear flow, The Journal of Chemical Physics 128 (2) (2008) 024901. doi:10.1063/1.2815766.

[40] D. J. Benson, Computational methods in lagrangian and eulerian hydrocodes, Computer Methods in Applied Mechanics and Engineering 99 (2-3) (1992) 235–394. doi:10.1016/0045-7825(92)90042-I.

[41] G. K. Batchelor, An Introduction to Fluid Dynamics, Cambridge University Press, Cambridge, 2000. doi:10.1017/CBO9780511800955.

[42] H. L. Goldsmith, S. G. Mason, The microrheology of dispersions, in: F. R. Eirich (Ed.), Rheology, Elsevier, 1967, pp. 85–250. doi:10.1016/B978-1-4832-2941-6.50008-8.

[43] F. P. Bretherton, The motion of rigid particles in a shear flow at low reynolds number, Journal of Fluid Mechanics 14 (02) (1962) 284. doi:10.1017/S002211206200124X.

[44] R. G. Cox, The motion of long slender bodies in a viscous fluid. part 2. shear flow, Journal of Fluid Mechanics 45 (04) (1971) 625. doi:10.1017/S0022112071000259.

[45] D. Bücheler, F. Henning, Hybrid resin improves position and alignment of continuously reinforced prepreg during compression co-molding with sheet molding compound, in: Proceedings of the 17th European Conference on Composite Materials, 2016.

[46] L. A. Feldkamp, L. C. Davis, J. W. Kress, Practical cone-beam algorithm, Journal of the Optical Society of America A 1 (6) (1984) 612. doi:10.1364/JOSAA.1.000612.

[47] M. R. Barone, D. A. Caulk, Kinematics of flow in sheet molding compounds, Polymer Composites 6 (2) (1985) 105–109. doi:10.1002/pc.750060208.

[48] M. Hohberg, L. Kärger, D. Bücheler, F. Henning, Rheological in-mold measurements and characterizations of sheet-molding-compound (SMC) formulations with different constitution properties by using a compressible shell model, International Polymer Processing 32 (5) (2017) 659–668. doi:10.3139/217.3556.

[49] H. Du Chung, T. H. Kwon, Invariant-based optimal fitting closure approximation for the numerical prediction of flow-induced fiber orientation, Journal of Rheology 46 (1) (2002) 169–194. doi:10.1122/1.1423312.

[50] Z. Püspöki, M. Storath, D. Sage, M. Unser, Transforms and operators for directional bioimage analysis: A survey, Advances in anatomy, embryology, and cell biology 219 (2016) 69–93. doi:10.1007/978-3-319-28549-8_3.

[51] L. Schöttl, K. Weidenmann, T. Sabiston, K. Inal, P. Elsner, Fiber bundle tracking method to analyze sheet molding compound microstructure based on computed tomography images, NDT and E International (submitted) (2019).

[52] A. G. Gibson, S. Toll, Mechanics of the squeeze flow of planar fibre suspensions, Journal of Non-Newtonian Fluid Mechanics 82 (1) (1999) 1–24. doi:10.1016/S0377-0257(98)00127-X.

[53] S. Toll, Packing mechanics of fiber reinforcements, Polymer Engineering & Science 38 (8) (1998) 1337–1350. doi:10.1002/pen.10304.